

# Observation of Pressure-Dependence in RF-Modulated Electron Beam Interactions With a Resonant Cylindrical Cavity

Joseph M. Connelly<sup>ID</sup>, Member, IEEE, John R. Harris<sup>ID</sup>, Senior Member, IEEE, J. Jack Watrous, Wayne E. Sommars, and Nathaniel P. Lockwood

**Abstract**—We present a series of experiments, in which the relativistic (5–20 MeV), low current (tens of milliamperes) electron beam from a microwave (2856 MHz) linear accelerator interacts with an air-filled cylindrical cavity whose pressure was varied from 1  $\mu$ Torr to 100 torr. The pulsed structure of the electron beam drives an electromagnetic resonance in the cavity, but the magnitude of this resonant signal was seen to collapse on a time scale depending on cavity pressure. This is believed to be due to beam-driven generation of conductive plasma inside the cavity, which detunes the center frequency of cavity mode the beam drives. The resonance collapse generally occurred on a 10–1000-ns time scale and exhibited a complex, nonmonotonic dependence on cavity pressure. Four distinct pressure regimes were exhibited: 1) at very low pressures, no collapse occurred; 2) at low pressures, a field-ionization-driven collapse occurred; 3) at moderate pressures, a combination of field and collisional ionization drove the collapse; and 4) at high pressures, collisional ionization dominated the collapse. These pressure bounds are generally highly dependent on beam and cavity parameters. This work broadly demonstrates that not only can an electron beam drive a resonant interaction in a radio frequency (RF) structure, but it can also generate a plasma inside of the structure that alters the nature of the interaction, potentially by an order of magnitude or more.

**Index Terms**—Cavity resonators, electron beams, electron linear accelerators (LINACs), plasma loaded waveguides.

## I. INTRODUCTION

PARTICLE beam interactions with resonant structures are of fundamental interest in a wide variety of accelerator and radio frequency (RF) source and diagnostic applications [4], [12], [19]. In particular, resonant cavities and waveguides can be electromagnetically excited when traversed by RF-modulated charged particle beams. In a recent series of experiments [6], [7], we explored such interactions under a number of experimental configurations, primarily using

Manuscript received 29 March 2022; revised 6 July 2022; accepted 11 July 2022. Date of publication 2 September 2022; date of current version 23 September 2022. This work was supported by the Air Force Research Laboratory Directed Energy Directorate and is approved for public release; distribution is unlimited. Public Affairs release approval under Grant #AFRL-2022-0286. The review of this article was arranged by Senior Editor C. A. Ekdaahl. (*Corresponding author: Joseph M. Connelly*)

Joseph M. Connelly, John R. Harris, and Nathaniel P. Lockwood are with the Air Force Research Laboratory Directed Energy Directorate, Kirtland AFB, Albuquerque, NM 87117 USA (e-mail: jconn2009@gmail.com).

J. Jack Watrous is with the Confluent Sciences LLC, Albuquerque, NM 87117 USA.

Wayne E. Sommars is with the Leidos Inc, Albuquerque, NM 87117 USA.

Color versions of one or more figures in this article are available at <https://doi.org/10.1109/TPS.2022.3192777>.

Digital Object Identifier 10.1109/TPS.2022.3192777

a 25-MeV S-band (2856 MHz) electron linear accelerator (LINAC) at the Idaho Accelerator Center [20]. These works showed that cavity electromagnetic resonances can be driven both by a primary beam of high energy electrons and from a secondary shower of lower energy electrons, produced by an incident X-ray beam. Such interactions are similar to system generated electromagnetic pulse (SGEMP), but with a semi-periodic pulse structure, such as that generated by a microwave LINAC [21], rather than a single impulse, such as that generated by a nuclear explosion [22]. SGEMP interactions with resonant structures have been explored elsewhere analytically [3], experimentally [13], and using both 2-D [2] and 3-D [1] electromagnetic particle-in-cell codes. Of considerable interest in these problems is the impact of initial gas density and ionization inside of the resonant structure [14] and variations in photon fluence, spectrum, and pulselength [17]. However, in all prior work, the X-ray and/or electron pulse is a single 1–10-ns burst [18], as opposed to a periodic sequence of micropulses (tens of picoseconds), which is the focus of this work.

We present and analyze a series of experiments using the Idaho Accelerator Center S-band LINAC and an air-filled cylindrical cavity resonant at S-band, where the air pressure inside the cavity varied from 1  $\mu$ Torr to 100 torr. Changing the pressure, and therefore the density of gas, inside the cavity dramatically altered the nature of the beam–cavity interaction, with the system demonstrating four distinct modes of operation at different pressure regimes. At pressures below 5 mTorr, the response of the cavity to the beam did not change significantly with pressure, but above this pressure, the beam ionizes the air inside the cavity producing plasma that shifts the center frequency of the cavity mode. Because the frequency content of the beam does not change, this mode shift decreases the magnitude of the resonant fields by as much as an order of magnitude. This shift generally occurs on a scale of tens to thousands of nanoseconds, depending on the cavity pressure and beam parameters. At relatively high pressures, electron collisional ionization is hypothesized to be the cause of the mode shift, and at relatively low pressures, field ionization appears to be the most likely source of the shift. In intermediate pressure regimes, both processes can significantly contribute to the collapse of the cavity resonance. The bounds on these pressure regimes are highly dependent on both the cavity geometry and beam parameters.

U.S. Government work not protected by U.S. copyright.

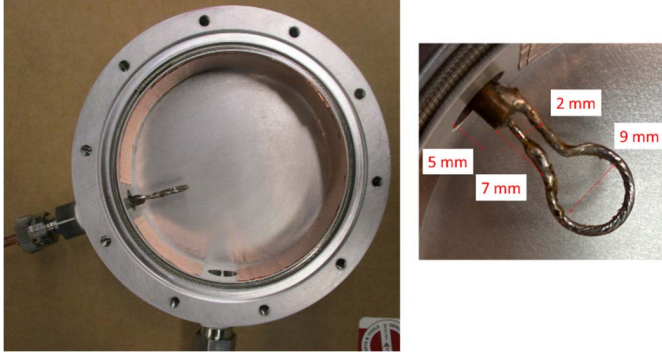


Fig. 1. Interior of the *S*-band cavity (left). Close-up of the B-dot geometry (right). The B-dot wire is 1 mm in diameter.

The remainder of this article is outlined as follows. Section II presents the *S*-band cavity, the LINAC, and the nuances of the vacuum pump setup and cavity  $S_{11}$ . Section III discusses the general experimental setup. We explore the cavity's pressure-dependent response while varying the beam energy, current, pulse duration, and repetition rate. We present the results of these experiments in Section IV. We show that the cavity's pressure response is well-captured by the envelope of the resonant field and identify four distinct regimes of operation. In Section V, we analyze and computationally model the beam–cavity interaction using Monte Carlo radiation transport methods and provide the estimates of collisional ionization rates at different pressures. We show that at low pressures, there is minimal collisional ionization of the air in the cavity from the beam, so any plasma must come from another source. In Section VI, we further discuss the experimental, analytic, and computational results and show agreement with a transition to collisional ionization at higher pressures. Finally, we provide concluding remarks in Section VII.

## II. APPARATUS

### A. Pressure-Tunable Cavity

The tunable *S*-band cavity, shown in Fig. 1, consisted of a machined cylindrical cavity with its TM01 mode tuned to approximately 2856 MHz [11]. The TM01 mode has only an axial electric field component and only an azimuthal magnetic field component. These fields are consistent with the electromagnetic fields produced by a relativistic electron beam propagating normal to the circular face of the cavity [10], so the TM01 mode is excited by a high-energy electron beam incident on the face of the cavity [6], [7]. No beam tube is present, and the electron beam is of sufficient energy to propagate through the cavity faces.

In order to obtain a TM01 mode at 2856 MHz, the diameter of the cavity was 8.0 cm. The cavity had a B-dot probe oriented to detect azimuthal magnetic fields, which enabled the measurement of the TM01 excitation. The center of the probe was located 16 mm from the perimeter of the cavity, as shown in Fig. 1. The perimeter of the cavity was lined with a copper tape in order to finely tune the center frequency of the cavity (no external tuning slug was used). The circular faces of the cavity were 13 mm thick and designed so that when the interior of the cavity was at 1 nTorr, the force due to the

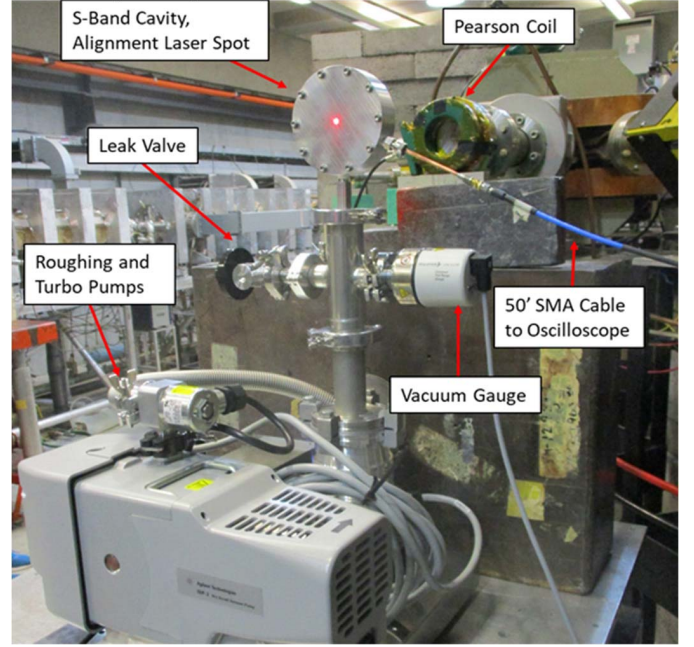


Fig. 2. General experimental setup used in these experiments, wherein a relativistic RF-pulsed electron beam interacts with a variable-pressure RF cavity (left).

pressure differential was not enough to significantly deform the cavity face. This was modeled using finite element analysis and experimentally confirmed by applying an equivalent force to the face plate, then verifying no changes to the cavity  $S_{11}$ . Additionally, a copper canted coil spring and rubber gasket ensured a proper electrical connection and vacuum seal, respectively, between the plate and the cylindrical tube portion of the cavity.

An additional port at the bottom of the cavity is connected to Aligent roughing and turbo pumps, a manually adjustable leak valve (Edwards LV10K), and a vacuum gauge (Pfeiffer PKR 251 and TPG 361). This setup, shown in Fig. 2, enabled the interior pressure of the cavity to be set to a given value. The gauge had to be kept out of the beam path, so the pressure measurement is taken just downstream of the cavity interior. To set the pressure of the cavity to 100 torr or lower, one or both of the vacuum pumps was on and the leak valve was adjusted until the cavity reached a steady state near the desired pressure. Above 100 torr, the pressure could be set by opening the leak valve and then closing it near the desired pressure, with both pumps off. Below 0.1 torr, both the roughing pump and the turbo pump were on; between 0.1 and 100 torr, only the roughing pump was used.

This produces four distinct regimes: 1) both vacuum pumps are evacuating the cavity and the leak valve is open (below 0.1 torr); 2) only the roughing pump is evacuating the cavity and the leak valve is open (0.1 to 100 torr); 3) neither pump is on and the leak valve is sealed; and 4) neither pump is on and the leak valve is open. In the first two cases, air enters the cavity via the leak valve, and molecules can exit the cavity via the vacuum pumps. However, in the third case, the cavity is a sealed system. To eliminate potential confounding variables, measurements were only taken up to 100 torr, so in all cases

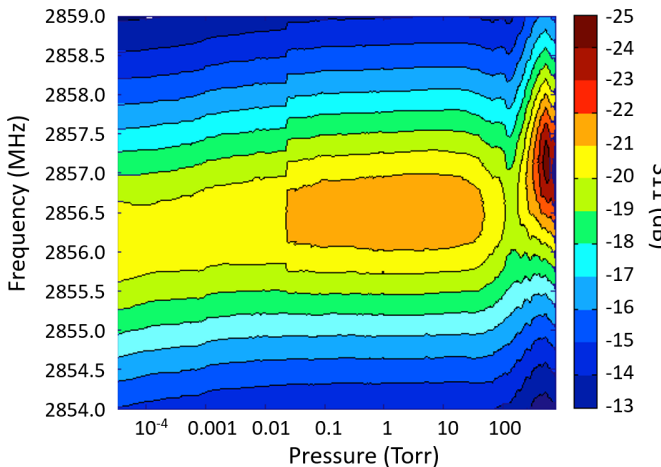


Fig. 3. Pressure-dependent  $S_{11}$  of the cylindrical cavity as measured through the B-Dot port. The full-width-half-max-bandwidth  $Q$  of the cavity is at least 650 for all  $\rho < 100$  torr, e.g., at 2  $\mu$ Torr, the 6-dB bandwidth at 2856 MHz is 4.38 MHz.

discussed herein, the leak valve is open with at least one pump on, corresponding to regimes 1) and 2).

#### B. Cavity $S_{11}$

$S_{11}$  of the cavity, as measured through the B-dot port, was recorded as a function of the cavity's internal pressure.  $S_{11}$  is the ratio of the reflected to incident power when a continuous-wave signal of a given frequency is inputted at the port, and it serves as a measure for the cavity's resonant frequencies and for how well electromagnetic waves of a given frequency couple into the probe. These  $S_{11}$  data, plotted in Fig. 3, were taken by first pumping the cavity down to 1  $\mu$ Torr, then increasing the pressure in a controlled manner, as described above, and recording the  $S_{11}$  data using a 4-GHz vector network analyzer (Keysight N9913A). Several noteworthy trends are present. First, there is a significant shift in  $S_{11}$  at pressures above 100 torr. Second, a discontinuity at 20 mTorr occurred when we inadvertently increased the pressure beyond the desired value and had to pump the cavity back down. The data are continuous both below and above 20 mTorr, which suggests that the cavity  $S_{11}$  is not consistent when the pressure is varied nonmonotonically, but it is consistent when the pressure increases monotonically. Hence, all experimental data, except for this  $S_{11}$  measurement, were taken by pumping the cavity down and then monotonically increasing the pressure. Even with these inconsistencies and hysteresis variations,  $S_{11}$  at 2856 MHz is between  $-20$  and  $-22$  dB at all pressures less than 100 torr.

The frequency shifting and other inconsistencies are presently hypothesized to be due to small shifts in the position of the B-dot probe as the pressure changes, likely due to the seal where the probe enters the cavity. As mentioned, deformations in the cavity face due to pressure differences had no discernable impact on  $S_{11}$ , and this was experimentally confirmed by directly applying weight to the cavity face while measuring  $S_{11}$ . The applied force was greater than the pressure differential force, and no variations was observed.

The  $S_{11}$  variation is significantly less in pressure regimes where one or both vacuum pumps are on, but there is a significant departure above 100 torr when both pumps are off and the leak valve is closed. These trends are consistent with the B-dot probe shifting slightly due to the pressure differential at the seal. The cavity  $S_{11}$  above 100 torr is another confounding variable (in addition to the different pump configurations), further justifying the restriction to pressures of at most 100 torr in the remainder of this article.

#### C. Accelerator

In these experiments, the Idaho Accelerator Center S-band (2856 MHz) electron LINAC was used [20]. The machine was tuned to produce an approximately monoenergetic beam between 5 and 20 MeV with 10–100 mA of current (averaged over the macropulse). In all configurations, the shot-to-shot variation, as measured by a downstream Pearson current transformer, was negligible.

An S-band klystron provided RF energy to fill the accelerating cavities, and the output of the klystron was altered to set the center energy of the beam. The electron energy spectrum was measured using a bending-magnet spectrometer. Energy spectra taken in this manner were approximate and indicated that the energy spread was within  $\pm 1\text{--}2$  MeV of the center energy, slightly lower at higher energies. The average beam current was controlled by adjusting the voltage applied to a gating grid in the thermionic electron gun and was measured with a Pearson coil located just downstream of the beam window. Adjusting the beam current in this manner can also affect the energy spectrum, since the cavity loading is varied.

The pulse format of a LINAC consists of short (tens of picoseconds) bursts of electrons, repeating at the fundamental frequency of the accelerator [21]. Such a signal will have frequency content at dc and at the RF fundamental frequency as well as the higher harmonics, which for the LINAC in these experiments, corresponds to 5712, 8568 MHz,...The electromagnetic fields produced by the beam will generally have a similar temporal structure to the beam current itself [10], so the beam's electromagnetic fields, particularly the azimuthal magnetic field (measured by the cavity B-dot probe), will have similar frequency content to the beam itself. However, since the S-band cavity's TM01 mode is resonant at 2856 MHz, the S-band electromagnetic fields were expected to dominate over the higher harmonics detected by the B-dot probe.

The axis of the beam in air downstream of the beam window was measured using glass plates and radiochromic film, both of which were darkened by the beam. A counterpropagating laser was aligned to the center of the beam spot indicated on the plates or film and subsequently used to ensure the placement of the cavity on the beam axis. The spot size of the beam was recorded using the film on both the upstream and downstream faces of the cavity. At 20 and 15 MeV, the upstream spot size was roughly 2 cm in diameter (3–4 cm for lower energies), and the downstream spot size generally encompassed the entire downstream face (8 cm), due to scattering from the interaction with the upstream face. The downstream spot size did not change significantly with pressure or other beam parameters.

### III. EXPERIMENTS

In all instances, the pressure-tunable cavity was placed so that its front face was 12 in downstream of the beam window and aligned, so that the center face of the cavity was normal to the beam axis and centered horizontally and vertically on the beam axis.

A typical experiment is proceeded as follows. The accelerator was tuned to produce the desired beam parameters (energy, current, pulse duration, and rep rate). In all instances, the cavity was initially brought down to  $<10^{-5}$  torr, and the cavity was brought up in pressure after each shot sequence. The cavity pressure was then recorded, the beam was turned on, and the cavity B-dot probe and Pearson coil signals were recorded using a 16-GHz Tektronic oscilloscope. Setting the pressure of the cavity required entering the accelerator shield vault and adjusting the leak valve. Four sets of experiments were performed, in which data were taken under a variety of cavity pressures and beam parameters.

In the first set of experiments, the current and pulse duration of the beam were fixed at 80 mA and 4  $\mu$ s, respectively, and the energy was set to 5, 9, 15, or 20 MeV ( $\pm 1\text{--}2$  MeV). In these experiments, the energy was set, and then, the pressure of the cavity was varied over its full range before moving onto the next energy. In the second set of experiments, the energy and pulse duration were fixed at 20 MeV and 4  $\mu$ s, respectively, and the average current was varied between 10 and 100 mA. In these experiments, the pressure of the cavity was set, and then, the current was varied over its full range before moving onto the next pressure. In the final set of experiments, the energy and current were fixed at 20 MeV and 80 mA, respectively, and the pulse format was modified to produce two pulses of varying duration and varying time between pulses. Similar to the second experiment, the pressure of the cavity was set, and then, the pulse format was varied over its full range before moving onto the next pressure.

In all configurations, the higher frequency content of the beam (5712, 8568 MHz, ...) was below the noise floor of the oscilloscope, since multiple attenuators were generally needed to measure the resonant S-band signal without damaging the oscilloscope. The measured B-dot signal was of the general form:  $x(t) \cos(2\pi f_0 t + \phi)$ , where  $f_0 = 2856$  MHz is the fundamental frequency of the accelerator,  $\phi$  is some phase angle, and  $x(t)$  is an envelope function that varies much slower than  $f_0$  (typically changes on the order of tens of nanoseconds). This is effectively the form of an amplitude modulated (AM) signal, wherein a high-frequency sinusoid carries a low-frequency envelope signal, so in postprocessing, standard AM demodulation techniques were used to extract the envelope  $x(t)$ . We verified that for all experimental configurations, the extracted envelope  $x(t)$  agreed extremely well with the raw B-dot data, which indicates that the envelope signal can accurately capture changes in the cavity signal that occur on the nanosecond time scale. As an example, Fig. 4 plots the B-dot signal along with its envelope and the Pearson coil trace, taken with the cavity pressure set to 5 mTorr. The probe voltage data are internally consistent throughout but,

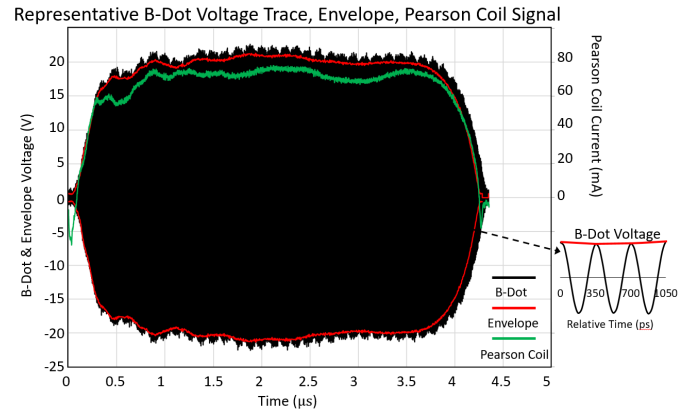


Fig. 4. Representative trace of the B-dot probe signal, which measured the azimuthal magnetic field, corresponding to the TM01 mode of the cavity. In this case, no cavity collapse occurs, and there is excellent agreement between the envelope of the probe signal and the Pearson-coil-measured envelope of the beam current.

because of a lack of calibration data, cannot readily be used to determine the fields in the cavity.

Furthermore, if we wish to compute the RF power dissipated at the oscilloscope, a useful metric for cavity response, it is straightforward to show that when  $x(t)$  is “slow” compared to  $f_0$ , the average power at the oscilloscope can be calculated by

$$\frac{1}{R\tau} \int_{-\infty}^{\infty} |x(t) \cos(2\pi f_0 t + \phi)|^2 dt \approx \frac{1}{2R\pi} \int_{-\infty}^{\infty} |x(t)|^2 dt \quad (1)$$

where  $x(t)$  is the oscilloscope voltage envelope signal,  $R = 50 \Omega$  is the terminating resistance of the oscilloscope, and  $\tau$  is the macropulse duration. This relationship specifically relies on the fact that  $x(t)$  is approximately constant over the RF period  $1/f_0$ , so that  $\int_{-\infty}^{\infty} |x(t)|^2 \cos(4\pi f_0 t) dt \approx 0$ . In these experiments  $1/f_0 \approx 350$  ps, and the measured envelopes varied on the order of tens of nanoseconds. We note that the oscilloscope power will be proportional to the RF power in the cavity but is not an absolute measurement of the cavity power.

### IV. EXPERIMENTAL RESULTS

In these experiments, we observed four distinct regimes of operation, distinguished by differences in the behavior of the envelopes of the RF signal detected by the cavity B-dot probe as a function of cavity pressure. These four regimes are depicted in Fig. 5 in the case of a 20-MeV, 80-mA beam and generally behave as follows.

- 1) Below 5 mTorr, there are slight variations in the magnitude of the cavity response, likely explained by the small shifts in the cavity  $S_{11}$ . However, the time structure of the envelope signals is nearly identical.
- 2) Between 5 mTorr and 1 torr, the cavity exhibits a collapse. As the pressure increases, both the time prior to collapse ( $T$ ) and the collapse time (the time between the start of the collapse and the signal reaching a steady state) decrease with increasing pressure,  $dT/d\rho < 0$ . The time prior to collapse versus pressure generally agrees well with a  $1/\rho$  fit.
- 3) Between 1 and 10 torr, the cavity still exhibits a collapse. However, as the pressure increases, both the time prior to

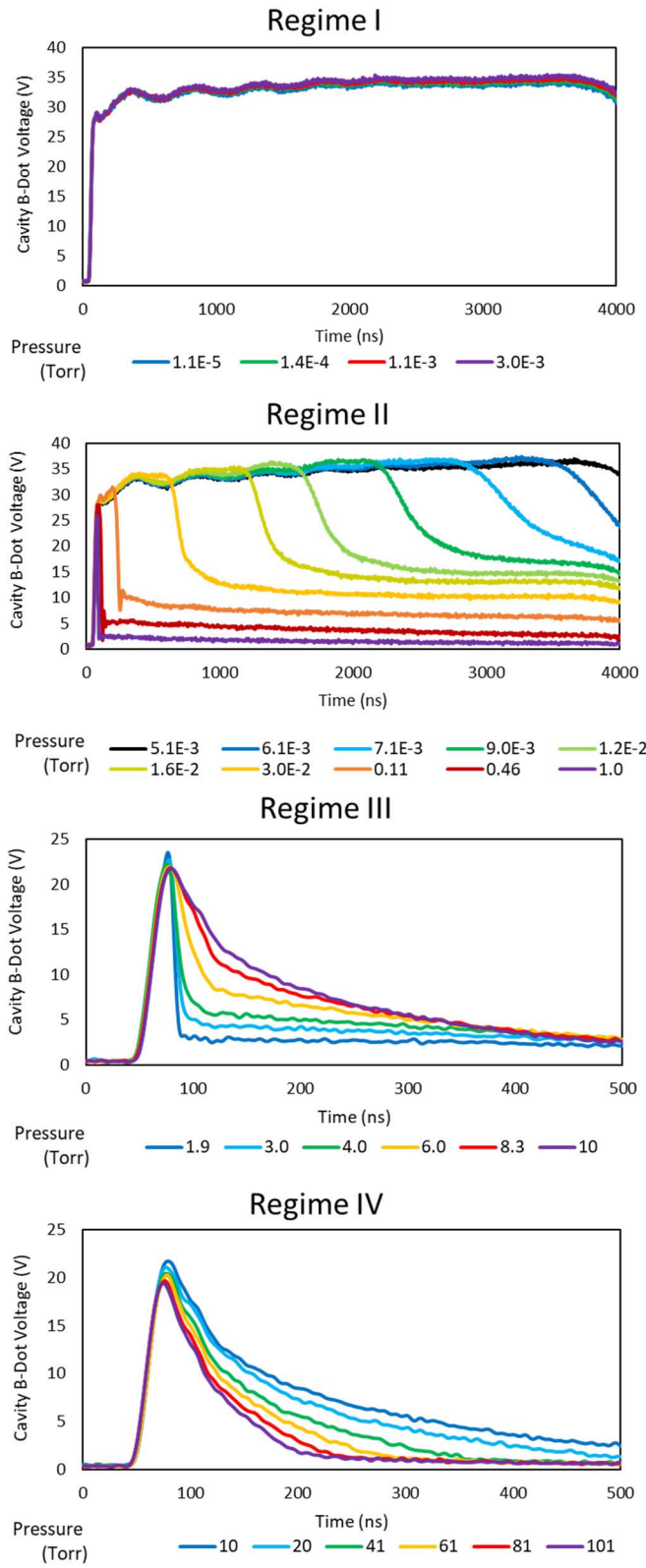


Fig. 5. Envelopes of the B-dot-measured cavity signal, from a 20-MeV, 80-mA electron beam, at various pressures. The plots correspond to different pressure regimes (displayed in torr), where trends in the collapse behavior are similar within a given regime.

collapse and the collapse time increase with increasing pressure,  $dT/d\rho > 0$ . This is the opposite relationship to that in regime II.

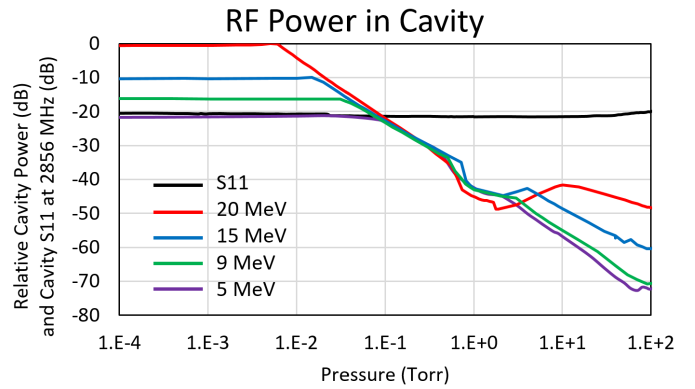


Fig. 6. Plot of the cavity RF power, for the four energies tested, and the measured cavity  $S_{11}$  (taken from Fig. 3) as a function of pressure.

- 4) Between 10 and 100 torr, the collapse time and time prior to collapse decrease,  $dT/d\rho < 0$ , and the magnitude of the signal decreases with increasing pressure.

In [16], single-pulse EMP interactions with air in four pressure regimes are discussed with similar pressure boundaries. In the low pressure regime, the cavity fields are not significantly altered by plasma. In an intermediate pressure region, the plasma is collisionless, and the EMP field magnitudes are reduced. In a transition region, the plasma transitions from collisionless to collision-dominated. Finally, at high pressures, the plasma is collision-dominated. It is noted that the pressure bounds on these regions are highly dependent on the characteristics of the radiation pulse, the size of the cavity, the magnitude of the field in the cavity, and other factors, and there is qualitative agreement in the experimental results from this work, in which the electron beam has a semi-period LINAC pulse structure.

#### A. Energy Dependence

The behavior when the beam energy is set to 5, 9, and 15 MeV is similar to the behavior at 20 MeV (with the current fixed at 80 mA in all cases); that is, the four pressure regimes are each still present. However, two key differences exist.

- 1) The signal magnitude increases with increasing energy.
- 2) The pressure at which the transition from regime I) to II) occurs increases as the energy decreases. However, the transitions between regimes II) and III) and regimes III) and IV) occur at similar pressures.

Fig. 6 shows the average RF power (dissipated at the oscilloscope, over the beam macropulse) as a function of pressure for each energy, alongside the cavity  $S_{11}$ . The RF power was computed using (1) (accounting for variations in the macropulse length  $\tau$ ).  $S_{11}$  was measured as in Section II-B and is included for reference.  $S_{11}$  only varies by a few decibels over the range of pressure, whereas the RF power of the beam-driven signal varies by as much as 50 dB.

RF power is not a perfect metric, as it does not capture the time-dependent nuances of the collapse. Nevertheless, this metric clearly captures the four pressure regimes at each energy, and the overall trends are similar, with two differences mentioned above. Regime I corresponds to the region of

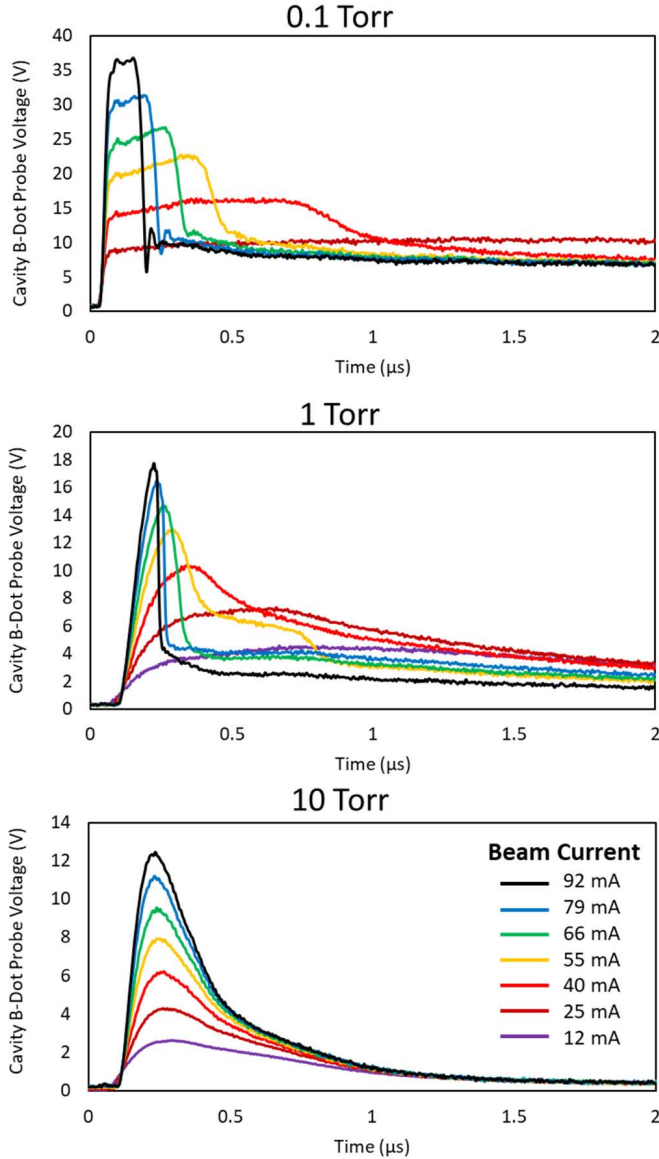


Fig. 7. Envelopes of the B-dot-measured cavity signal, from 20-MeV electron beams with varying currents.

constant cavity power, regime II corresponds to the log-linear decrease in cavity power (rate of change independent of beam energy), regime III corresponds to the break in the log-linear relationship, and regime IV corresponds to a return to a log-linear relationship (rate of change dependent on beam energy). Because the energy spectra were approximate and long tails were present around the center energy, these results are taken as qualitative rather than quantitative.

#### B. Current Dependence

When the cavity pressure was  $<5$  mTorr, changing the current resulted in a linear variation in the magnitude of the cavity response and no collapses occurred. The steady-state envelope voltage (in V) is well approximated by  $0.41 \cdot I$ , where  $I$  is the initial current in millampere.

Fig. 7 shows the cavity signal envelopes for varying beam currents at representative pressures (0.1, 1, and 10 torr). As the current changes, not only does the magnitude of the

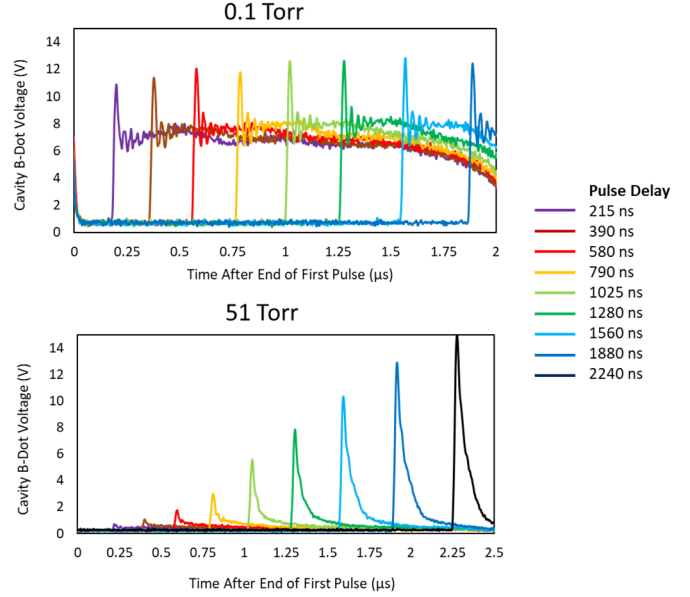


Fig. 8. Envelopes of the B-dot-measured cavity signal, from 20-MeV, 80-mA electron beams, with varying time between pulses. The cavity's response to the first pulse had reached a fully collapsed state and is omitted to improve readability. The collapse is similar to the corresponding pressures in Fig. 5.

cavity signal change, but the collapse properties also vary. At 0.1 and 10 torr (regimes II and IV), both the time to collapse and the collapse time decrease with current. That is, the collapse becomes “sharper” as the current increases. At 1 torr (regime III), the trend is similar, but the pulse shape prior to collapse also significantly varies with current.

#### C. Repetition Rate and Recoup Time

The previous experiments have demonstrated that the cavity collapse occurs on the order of tens to thousands of nanoseconds. Since this is a transient effect, presumably due to a conductive plasma detuning a mode, the cavity mode recovers to its initial state given enough time between beam shots. In order to study how the cavity recuperates, we varied the time between pulses of the beam in two ways.

First, the repetition rate of the accelerator was varied from 0.1 to 100 Hz, the maximum rep-rate of the accelerator. In these cases, there was no dependency on time between pulses, i.e., the cavity full recuperated from any previous shots by the time the next macropulse arrives.

Second, the beam macropulse was split into two shorter pulses with variable timing (10–2500 ns) between the pulses. In these experiments, the first pulse was long enough for the cavity to reach an equilibrium, collapsed state. Fig. 8 shows the cavity response to the second pulse for two representative cases, where the pressure was set to 0.1 and 51 torr, respectively. At 0.1 torr, the structure of the cavity's response to the second pulse is independent of the time between pulses, indicating that no recuperation has occurred. However, at 51 torr, the magnitude of the cavity's response to the second pulse increases with time between pulses. This indicates that the cavity has only partially recuperated from its collapse in this case. Experimental limitations prevented testing recoup times between 3  $\mu$ s and 10 ms.

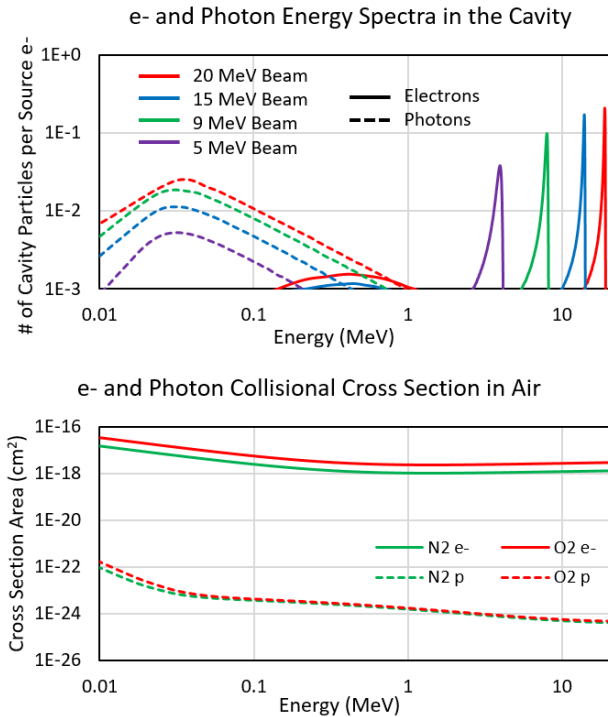


Fig. 9. Computed photon and electron energy spectra inside the *S*-band cavity (top), assuming varying initial electron energy, as calculated using the EMLOW package in GEANT4 (bottom). The collisional cross section for high-energy photons and electrons (calculated using the RBEB model), respectively.

## V. SIMULATION AND ANALYSIS

The previous section demonstrated four clear regimes. In this section, we explore computational models of the beam–cavity interaction to better understand the regime transitions.

### A. Beam Spectrum Inside the Cavity

A series of GEANT4 [23] simulations were performed in order to determine the electron and photon energy spectra inside the cavity. The EMLOW physics package was used to account for scattering, Bremsstrahlung, photoemission, pair production, and other processes that can be captured in a Monte Carlo radiation transport code, like GEANT4. We performed simulations with an initial electron beam energy of 20, 15, 9, or 5 MeV. The electron beam begins as a pencil beam propagating in vacuum, then passes through a 1-mil Ti window, and then through 10 cm of air. Two 13-mm-thick aluminum plates were separated by 26 mm of vacuum to mimic the geometry of the cavity. The electron and photon fluences through the center of the cavity were recorded as a function of particle energy. Both the electrons and photons can potentially interact with and ionize the air inside the cavity through collisions. The resulting energy spectra inside the cavity are shown in Fig. 9.

The electrons lose approximately 1 MeV of energy passing through the aluminum plate, and the energy spectra spread out slightly. The beam current also attenuates when passing through the aluminum plate. This effect is more pronounced at lower energies. So while the current just downstream of the beam window was the same for the energy-dependent

TABLE I  
AVERAGE NUMBER OF ELECTRON AND PHOTON COLLISIONS PER SOURCE ELECTRON INSIDE OF THE CAVITY

Initial Energy	Average e- Collisions per Source e-	Average Photon Collisions per Source e-
20 MeV	$0.121 \cdot \rho$ [Torr]	$1.20 \cdot 10^{-7} \cdot \rho$ [Torr]
15 MeV	$0.117 \cdot \rho$ [Torr]	$1.27 \cdot 10^{-7} \cdot \rho$ [Torr]
9 MeV	$0.102 \cdot \rho$ [Torr]	$1.32 \cdot 10^{-7} \cdot \rho$ [Torr]
5 MeV	$0.0651 \cdot \rho$ [Torr]	$1.11 \cdot 10^{-7} \cdot \rho$ [Torr]

experiments, the current in the cavity was about 103%, 102%, 95.4%, and 64.8% of the measured 80-mA current for 20, 15, 9, and 5 MeV, respectively. These quantities were computed by integrating the electron spectra curves to obtain the total number of electrons passing through the cavity per source electron.

The photon energy spectrum, produced primarily by Bremsstrahlung X-rays from the electron–aluminum interaction, is fairly consistent across the different electron energies. The energy spectra peak below 10 keV, with a long tail up to roughly 1 MeV. In all cases, there are about 0.2 photons in the cavity per source electron (obtained by integrating the spectra).

### B. Collisional Ionization

Fig. 9 also shows the collisional cross-sectional areas of N<sub>2</sub> and O<sub>2</sub> for high-energy electrons, as calculated by the relativistic binary encounter Bethe (RBEB) equation [5, eq. (19)], and for photons, as calculated using the mass attenuation coefficients [24] (accounting for photoelectric absorption, scattering, and pair production). The mean free path, i.e., the average distance a particle propagates before undergoing a collision, is given by  $\sigma(T) \cdot N$ , where  $\sigma(T)$  is the energy-dependent cross section and  $N = 2.504 \cdot 10^{19} \cdot ((\rho \text{ [torr]})/760) \text{ cm}^{-3}$  is the air number density in the cavity. The mean free path of electrons in air is computed for various pressures in Fig. 10 and is on the order of the cavity length  $L = 2.6 \text{ cm}$  when the pressure  $\rho$  is between 1 and 100 torr. The mean free path of photons in air is much larger than  $L$  for all pressures studied here. The average number of ionizing collisions an electron of given energy experiences inside the cavity is the mean free path multiplied by the length of the cavity

$$\sigma(T) \cdot N \cdot L. \quad (2)$$

Since  $\sigma$  depends on energy and the beam–cavity interaction produces a spectrum of energies, the average number of collisions, for each particle species, per source electron is then given by

$$\int \Psi(T) \cdot \sigma(T) \cdot N \cdot L dT \approx 8.566 \cdot 10^{16} \cdot \rho \text{ [torr]} \cdot \int \Psi(T) \cdot \sigma(T) dT \quad (3)$$

where  $\Psi(T)$  is the particle energy spectrum in the cavity. The integral on the right-hand side can be computed using the data in Fig. 9, specifically by multiplying the spectrum curves by the cross-sectional curves and integrating. The computed average number of electron and photon air collisions inside the cavity are shown in Table I for each initial electron energy as a function of pressure.

From these results, we can conclude that ionization from secondary photons is negligible at pressures of interest, since

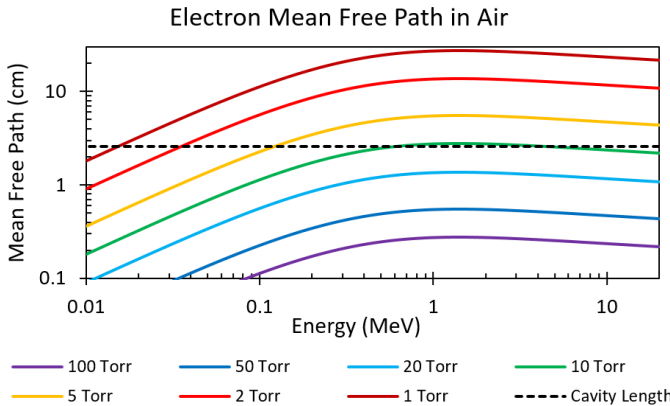


Fig. 10. Mean free path of electrons in air versus energy for various pressures, as calculated using the RBEB model [5]. The cavity length is also shown. The number of ionizing collisions in the cavity per source electron is approximately the ratio of the cavity length (2.6 cm) to the mean free path.

even at  $\rho = 760$  torr, the average number of photon collisions per source electron is at most  $10^{-4}$ , and this includes interactions that do not produce ions, such as scattering. The number of ionizing electron collisions per source electron is highly pressure-dependent and sometimes will be much less or much greater than the number of electrons in the cavity.

When the number of collisions per source electron is much less than the number of beam electrons in the cavity, the electromagnetic fields produced by the electron–cavity interaction will dominate any effects of the collisionally ionized air in the cavity, i.e., the ion density is much less than the electron beam density. On the other hand, when the number of collisions per source electron is comparable or greater than the number of electrons in the cavity, the ionized air molecules can significantly alter the net charge/current and thus the electromagnetic fields in the cavity. For each energy, the ratio of collisions per cavity electron is reasonably approximated (from Table I) by  $0.1 \cdot \rho(\text{torr})$ .

This ratio is  $\ll 1$  (i.e., negligible collisional ionization) when the pressure  $<\sim 1$  torr and is  $\gg 1$  (i.e., more ions than beam electrons) when pressure  $>\sim 100$  torr (i.e., the mean free path is much less than or much greater than the cavity length). These bounds agree well with the transition from regime II to III for each energy ( $\sim 0.7$  torr), where the collapse behavior begins to exhibit different trends with pressure. These bounds will generally depend on the length of the cavity, but from them, we can conclude that below  $\sim 1$  torr, collisional ionization within this particular cavity does not significantly impact the beam–cavity interaction.

Also of note is that in all experimental configurations, the number density of the air molecules in the cavity is much greater than the electron density of the beam. Specifically, for a 4  $\mu\text{s}$ , 100-mA beam with 1 cm radius, the electron density is approximately  $6.6 \cdot 10^6 \text{ e}/\text{cm}^3$ . On the other hand, even at 1  $\mu\text{Torr}$ , the air number density in the cavity is approximately  $4 \cdot 10^{10} \text{ molecules}/\text{cm}^3$ . This suggests that the number of ions in the cavity can easily overwhelm the charge density of the beam, when each beam electron undergoes multiple ionizing collisions.

## VI. DISCUSSION

While there were small variations in the cavity  $S_{11}$  with pressure, they are highly unlikely to be the cause of the time-dependent behavior of the voltage collapse. Additionally, the RF power varies with pressure by as much 50 dB, whereas  $S_{11}$  varied with pressure by no more than 2 dB.

The voltage collapse cannot also be attributed to changes in the vacuum pump setup. We restricted data collection to  $<100$  torr to avoid comparing cases where the leak valve was open and at least one vacuum pump was on (the cavity is actively being evacuated) to cases where the leak valve was closed and no vacuum pump was on (the cavity is a closed system). Additionally, the turbo pump was turned on to attain pressures less than 0.1 torr, and there were no regime transitions or deviation from trends near this pressure.

The results of this work indicate that the most likely explanation for the cavity collapse is beam-driven (collisional and field) ionization that forms a plasma in the cavity. The interaction of the cavity, the collision and field-induced plasma, and the beam itself is a complex air chemistry and electrodynamics problem [26]. Full analysis is outside of the scope of the present article and a subject of future work.

However, a simple model of this plasma is to treat it as a conductor. It is known that even small perturbations in microwave cavities can significantly alter  $S_{11}$  of the cavity [25]. If a plasma is introduced in the cavity, the center frequency of the cavity mode will change. If a plasma is formed more rapidly in the cavity (due to increased ionization rate), the voltage will collapse more rapidly. When there are multiple sources of ionization, the plasma interactions are more complicated, which is consistent with the nonmonotonic behavior of regimes II, III, and IV.

The analysis and modeling in Section V suggest that collisional ionization does not significantly contribute to a plasma below 1 torr (corresponding to the transition from regime II to III). However, a voltage collapse is still present in regime II, suggesting that some other effect is driving the plasma formation. The collapse trends are consistent in regime II across the electron energies tested. The lower pressure bound for regime II generally varies with beam energy and generally appears to depend on the RF power in the cavity. In particular, in Fig. 6, for each energy, the cavity enters regime II when the pressure (in torr) is equal to

$$10^{-\frac{P_{RF} [\text{dB}] + 40}{18}}$$

and in regime II, the cavity power (in decibel) has excellent agreement with the fit  $-18 \cdot \log_{10} \rho - 40$ .

To bound the field strength in the cavity, consider a beam passing through a vacuum pillbox cavity with a negligible face plate interaction. Since  $Q \approx 650$ , the shunt impedance of the pillbox cavity of diameter 8 cm and length 2.6 cm is roughly 44  $\text{k}\Omega$  [11]. The maximum voltage across the gap (ignoring coupling inefficiencies) is then on the order of  $R_{\text{shunt}} \cdot I_B \approx 4 \text{ kV}$ . With a gap of  $L = 2.6 \text{ cm}$ , the resultant field is substantially less than the atmospheric breakdown field threshold of  $\sim 30 \text{ kV/cm}$ , but certain instances of Paschen's law can yield breakdown in sub-torr gases with  $\sim \text{cm}$  gaps and

ac voltages on the order hundreds of volts [27]. Further analysis of the effect of field-driven ionization and its impact on the time-dependent cavity collapse is a subject of future work.

The transitions between regimes II and III and regimes III and IV occurred at similar pressures across all energies. This is supported by the numerical analysis in Section V, where, at all energies, collisional ionization starts to become relevant around 1 torr and produces many more ions than there are beam electrons by 100 torr.

The current-varying experiments suggest that the collapse can be accelerated by introducing more current in the cavity. This is also consistent with a beam-driven plasma, particularly one primarily dependent on the beam-induced RF power in the cavity at lower pressures. Prior to collapse, the resonant cavity signal varies linearly with current, so a higher current can yield a higher field ionization rate. The energy-varying experiments are also consistent with this trend. Section V indicates that fewer electrons pass through the cavity at lower energies, which is consistent with shift in the bounds on regime II, since there is less RF power in the cavity when the current is lower.

The multiple pulse experiments indicate recuperation after collapse is a complicated process. At 51 torr, the cavity begins to recuperate on the order of hundreds of nanoseconds, but at 0.1 torr, recuperation does not occur even after 2 ms. However, in all cases, the cavity has fully recuperated after 10 ms. The results of these experiments are also generally consistent with a plasma formed in the cavity. Unfortunately, experimental limitations prevented further exploration of recuperation times between 3 and 10 ms.

## VII. CONCLUSION

This work has demonstrated that a relativistic RF-pulsed electron beam can not only drive resonant interactions in an RF cavity, but it can also generate plasma inside of an RF cavity that can detune the cavity modes and cause the resonant signal to collapse. This interaction introduces a physics-rich environment, a full model of which is outside of the scope of this work, and has significant implications for beam–cavity interactions. If the plasma detuning is not accounted for the cavity, RF power can be underpredicted by 50 dB or more.

The results of the analysis and experiments in this work, wherein we consider a microwave-modulated electron LINAC beam, are broadly consistent with results from the literature, which explore single-pulse SGEMP interactions with cavities held at various pressures [1], [2], [3], [13], [14], [17], similarly demonstrating four regimes of pressure-dependence corresponding to no plasma, a field-driven plasma, collision- and field-driven plasma, and a collision-driven plasma. The experimental and analytic results from this work indicate that these regime boundaries will generally depend on beam parameters, as well as the cavity geometry. Determining generalized boundaries on these regimes as a function of cavity and beam parameters is a potential subject of future work. Such results would provide back of the envelope estimates of whether beam-driven plasma can be ignored in a given interaction and how to account for it when it cannot be. The cavity response to the beam provides some limited information about the plasma inside of it, but further study is needed to better understand these interactions in general.

## REFERENCES

- [1] Z. Xu, C. Meng, Y. Jiang, and P. Wu, “3-D simulation of cavity SGEMP interference generated by pulsed X-rays,” *IEEE Trans. Nucl. Sci.*, vol. 67, no. 2, pp. 425–433, Feb. 2020.
- [2] A. J. Woods and E. P. Wenaas, “SGEMP geometry effects,” *IEEE Trans. Nucl. Sci.*, vol. NS-22, no. 6, pp. 2374–2380, Dec. 1975.
- [3] K. S. H. Lee and L. Marin. (Sep. 1974). *SGEMP for Resonant Structures*. Theoretical Note 199. Accessed: Jan. 24, 2022. [Online]. Available: <https://ece-research.unm.edu/summa/notes/TheoreticalPDFs/TN199.pdf>
- [4] M. Siman-Tov, J. G. Leopold, Y. P. Bliokh, and Y. E. Krasik, “Periodic bunches produced by electron beam squeezed states in a resonant cavity,” *Phys. Plasmas*, vol. 27, no. 8, Aug. 2020, Art. no. 083103.
- [5] Y.-K. Kim, J. P. Santos, and F. Parente, “Extension of the binary-encounter-dipole model to relativistic incident electrons,” *Phys. Rev. A, Gen. Phys.*, vol. 62, no. 5, Oct. 2000, Art. no. 052710.
- [6] J. R. Harris, C. N. Harris, R. B. Miller, and N. T. Myers, “Propagation and detection of RF-modulated electron and X-ray beams in air,” *J. Appl. Phys.*, vol. 123, no. 22, Jun. 2018, Art. no. 223303.
- [7] J. R. Harris and R. B. Miller, “Propagation of modulated electron and X-ray beams through matter and interactions with radio-frequency structures,” *J. Appl. Phys.*, vol. 123, no. 8, Feb. 2018, Art. no. 083302.
- [8] R. B. Miller, P. McChesney, J. R. Harris, and N. Myers, “Evolution of the micropulse structure of an electron beam propagating in air,” *J. Appl. Phys.*, vol. 125, no. 3, Jan. 2019, Art. no. 034902.
- [9] J. Connelly, J. Harris, K. Folkman, B. Berls, C. O’Neill, and J. Stoner, “Microwave radiation from interactions of modulated electron beams with solid matter,” *AIP Adv.*, vol. 10, no. 7, Jul. 2020, Art. no. 075008.
- [10] J. M. Connelly and J. R. Harris, “Microwave radiation from propagating relativistic modulated electron beams,” *J. Radiat. Effects Res. Eng.*, vol. 39, no. 1, pp. 19–33, Apr. 2021.
- [11] D. M. Pozar, *Microwave Engineering*, 2nd ed. New York, NY, USA: Wiley, 1998, Sec. 6.8, pp. 340–344.
- [12] T. R. Pusch, F. Frommberger, W. C. A. Hillert, and B. Neff, “Measuring the intensity and position of a pA electron beam with resonant cavities,” *Phys. Rev. Special Topics-Accel. Beams*, vol. 15, no. 11, Nov. 2012, Art. no. 112801.
- [13] A. J. Woods, M. J. Treadaway, S. Nunan, and D. Higgins, “Air-enhanced SGEMP response—An experimental and analytical investigation,” *IEEE Trans. Nucl. Sci.*, vol. NS-29, no. 6, pp. 1793–1797, Dec. 1982.
- [14] A. J. Woods, W. E. Hobbs, and E. P. Wenaas, “Air effects on the external SGEMP response of a cylinder,” *IEEE Trans. Nucl. Sci.*, vol. NS-28, no. 6, pp. 4467–4478, Dec. 1981.
- [15] A. F. Aleksandrov, V. L. Bychkov, L. P. Grachev, I. I. Esakov, and A. Y. Lomteva, “Air ionization in a near-critical electric field,” *Tech. Phys.*, vol. 51, no. 3, pp. 330–335, Mar. 2006.
- [16] W. F. Rich and T. A. Stringer, “System-generated electromagnetic pulse and spacecraft charging effects: A review of the technology as applied to system hardening problems,” *IEEE Trans. Nucl. Sci.*, vol. NS-27, no. 6, pp. 1523–1528, Dec. 1980.
- [17] A. J. Woods and E. P. Wenaas, “Scaling laws for SGEMP,” *IEEE Trans. Nucl. Sci.*, vol. NS-23, no. 6, pp. 1903–1908, Dec. 1976.
- [18] R. H. Stahl, D. C. Osborn, and E. P. Wenaas, “SGEMP simulation experiments with electron beams,” *IEEE Trans. Nucl. Sci.*, vol. NS-23, no. 6, pp. 1975–1981, Dec. 1976.
- [19] M. Resier, *Theory and Design of Charged Particle Beams*. Weinheim, Germany: Wiley, 2008.
- [20] Idaho Accelerator Center. *Accelerator Information*. Accessed: Jan. 24, 2022. [Online]. Available: <https://www.isu.edu/iac/facilities-scheduling/accelerator-information/>
- [21] T. Wangler, *Principles of RF Linear Accelerators*. Weinheim, Germany: Wiley, 2008.
- [22] C. Longmire, “Electromagnetic pulse generated by nuclear explosions,” in *Proc. Antennas Propag. Soc. Int. Symp.*, 1975, pp. 435–438.
- [23] S. Agostinelli *et al.*, “GEANT4—A simulation toolkit,” *Nucl. Instrum. Methods Phys. Res. A, Accel., Spectrometers, Detectors Associated Equip.*, vol. 506, no. 3, pp. 250–303, Jul. 2003.
- [24] NIST. *X-Ray Mass Attenuation Coefficients*. Accessed: Jan. 24, 2022. [Online]. Available: <https://physics.nist.gov/PhysRefData/XrayMassCoef/chap2.html>
- [25] T. G. Jurgens, “Equations for bead-pull cavity measurements,” Fermilab Nat. Accel. Lab., Batavia, IL, USA, Tech. Rep. Fermilab-LU-159, 1990.
- [26] B. Freemire *et al.*, “Pressurized RF cavities in ionizing beams,” *Phys. Rev. Accel. Beams*, vol. 19, no. 6, Jun. 2016, Art. no. 062004.
- [27] C. E. Muehe, “AC breakdown in gases,” MIT Lincoln Lab., Lexington, MA, USA, Tech. Rep., 380, Feb. 1965.